ISSN 1063-7834, Physics of the Solid State, 2019, Vol. 61, No. 6, pp. 1052–1061. © Pleiades Publishing, Ltd., 2019.
Russian Text © The Author(s), 2019, published in Fizika Tverdogo Tela, 2019, Vol. 61, No. 6, pp. 1128–1137.

FERROELECTRICITY

Study of the Physical Properties and Electrocaloric Effect in the $BaTiO_3$ Nano- and Microceramics

A. V. Kartashev[a, b, *], V. S. Bondarev[a, c], I. N. Flerov[a, c], M. V. Gorev[a, c], E. I. Pogorel'tsev[a, c], A. V. Shabanov[a], M. S. Molokeev[a, c], S. Guillemet-Fritsch[d], and I. P. Raevskii[e]

[a] *Kirensky Institute of Physics, Krasnoyarsk Scientific Center, Siberian Branch, Russian Academy of Sciences, Krasnoyarsk, 660036 Russia*

[b] *Krasnoyarsk State Pedagogical University, Krasnoyarsk, 660049 Russia*

[c] *Siberian Federal University, Institute of Engineering Physics and Radio Electronics, Krasnoyarsk, 660041 Russia*

[d] *CIRIMAT Laboratory, University of Toulouse, Toulouse, 31062 France*

[e] *Southern Federal University, Research Institute of Physics, Rostov-on-Don, 344090 Russia*

**e-mail: akartashev@yandex.ru*

Received December 8, 2018; revised December 8, 2018; accepted January 15, 2019

Abstract—The specific heat, thermal expansion, permittivity, and electrocaloric effect in bulk of $BaTiO_3$ (BT) samples in the form of nano- (nBT-500 nm) and micro- (mBT-1200 nm) ceramics fabricated using spark plasma sintering and solid-state plasma techniques have been investigated. The size effect has been reflected, to a great extent, in the suppression of the specific heat and thermal expansion anomalies and in the changes in the temperatures and entropies of phase transitions and permittivity, and a decrease in the maximum intensive electrocaloric effect: $\Delta T_{AD}^{max} = 29$ mK ($E = 2.0$ kV/cm) for nBT and $\Delta T_{AD}^{max} = 70$ mK ($E = 2.5$ kV/cm) for mBT. The conductivity growth at temperatures above 360 K leads to the significant irreversible heating of the samples due to the Joule heat release in the applied electric field, which dominates over the electrocaloric effect.

DOI: 10.1134/S1063783419060088

1. INTRODUCTION

An important problem of condensed matter physics is obtaining information about the effect of fields of different physical natures on the sequence, entropy, and temperature of the phase transitions in solids. This is related, in particular, to the search for new materials promising for application in coolers that operate on the basis of the caloric effects in solids. A promising direction in the solid-state cooling is based on the electrocaloric effect, which is the simplest to implement and thereby has stimulated a significant increase in the number of studies on it [1–3].

The electrocaloric effect (ECE) is the change in the temperature or entropy in an applied electric field under adiabatic or isothermal conditions, respectively. As was shown in [4], the change in the temperature of a solid-state cooling agent by 2–5 K due to the ECE is sufficient to create a more energy-efficient and commercially accessible cooling system as compared with the available vapor-liquid refrigerators. Since the ECE is proportional to the temperature derivative of polarization $(dR/dT)_E$, its largest value can be implemented in ferroelectric materials near the phase transition in strong electric fields ($E > 200$ kV/cm). However, the electric breakdown in bulk ferroelectrics occurs, as a rule, already in fields up to 60 kV/cm, which leads to their destruction. On the other hand, thin ferroelectric films withstand stronger electric fields (1000–2000 kV/cm) [5–7]. For this reason, in the $PbZr_{0.95}Ti_{0.05}O_3$ films, a giant intensive ECE $\Delta T_{AD}^{max} = 12$ K was observed in an electric field of $E = 480$ kV/cm [8]. However, thin films have a small thermal mass and cannot effectively remove the electrocaloric heat.

The other type of ferroelectric materials promising for obtaining high ECE values is multilayer structures [9, 10]. They are stable against strong electric fields due to the alternation of thin (~3 μm) layers in their volume; in addition, they have a large thermal mass and, therefore, high cooling power. Unfortunately, multilayer structures exhibit low ECE values ($\Delta T/\Delta E = 1.7$ mK cm/kV) as compared to bulk polycrystalline ferroelectrics ($\Delta T/\Delta E = 30$ mK cm/kV) due to the impact of size effects on the parameters of phase transitions and physical properties [11, 12].

In view of the aforesaid, the question naturally arises how to enhance the electrocaloric coefficient and breakdown field in ferroelectric materials.

As was shown recently [13–15], the micro- and nanoceramics size strongly affects the stability of a material against the electrical breakdown. The studies of nanocrystalline oxide ceramic materials, in particular, barium titanate $BaTiO_3$ ceramics [16, 17], demonstrated a significant dependence of the parameters of phase transitions and physical properties on the synthesis conditions and grain size [18]. For example, a decrease in the film thickness from 1100 to 20 nm leads to a decrease in the ferroelectric phase transformation temperature from 395 to 371 K. In this case, the specific heat anomaly is spread and the polarization decreases from 11 to 4 $\mu C/cm^2$. Therefore, the problem of controlling the grain size during the formation of ceramic materials becomes crucially important. A study of the influence of the size effects, thermal history of materials, and methods for their fabrication on the electrical and thermodynamic characteristics is important for finding the conditions optimal for increasing the breakdown electric field and electrocaloric efficiency of solid cooling agents based on micro- and nanoceramic ferroelectrics and multilayers.

In this work, we present the results of investigations of the thermodynamic (specific heat and thermal expansion), structural, and dielectric properties and the ECE in $BaTiO_3$ micro- and nanoceramics in a wide temperature range. The integrated approach to studying the thermal and caloric properties makes it possible to obtain important information about the nature of physical phenomena in micro- and nanoceramic materials, temperatures of phase transitions, entropy and strain parameters, and caloric efficiency.

2. EXPERIMENTAL

$BaTiO_3$ nanopowders were synthesized by the oxalate precipitation. The procedure was described in detail in [19]. The precursors used were Prolabo $BaCl_2 \cdot 2H_2O$ and $TiOCl_2$. The precursors were weighed in a certain proportion to control the powder stoichiometry, dissolved in water, and added to the ethanol solution of oxalic acid. The $BaTiO_3$ powder was obtained after calcination in air at 850°C for 4 h. The powders were placed in a graphite crucible with an inner diameter of 8 mm and subjected to spark plasma sintering (SPS) in a Sumimoto 2080 SPS system under a pressure of 75 MPa at 1150°C for 3 min at a heating rate of 50 C/min) and then rapidly cooled. The obtained SPS grains were annealed in an oxidizing atmosphere at 850°C for 48 h to restore the oxygen stoichiometry. The main advantages of the SPS technique over conventional sintering are the lower temperature and significantly shorter time of the process, as well as the possibility of obtaining a very high (~97%) density of ceramics at small grain sizes.

The $BaTiO_3$ (mBT) microceramic was obtained using a conventional solid-state technology. The stoichiometric $BaCO_3$ and TiO_2 amounts with a main substance content of more than 98% were thoroughly mixed in distilled water. After drying the obtained mixture, the solid-phase synthesis was performed in two four-hour stages at 1100 and 1150°C, respectively. After each stage, the reaction product was crushed and stirred. Before the final sintering, the obtained powder was pressed into discs with a diameter of 30 mm and a height of 10 mm at 100 MPa. A three-percent aqueous solution of polyvinyl alcohol was used as a plasticizer. After burning out the plasticizer by slow heating to 600°C, sintering at 1330°C for 3 h in a closed alumina crucible on a corrugated ZrO_2 ceramic substrate was carried out. After sintering, the temperature was reduced at a rate of 100°C/h to 800°C; then, the samples were slowly cooled in a furnace to room temperature. The density of the obtained ceramics was 92.5% of the theoretical value.

The composition and quality of the samples were controlled using electron microscopy and X-ray diffraction analysis.

The structural morphology of the $BaTiO_3$ ceramic surface was studied on a Hitachi TM3000 scanning electron microscope (SEM) (Hitachi High-Technologies Co., Ltd., Tokyo, Japan). A typical SEM image of the $BaTiO_3$ nanoceramics (nBT) is shown in Fig. 1a. One can clearly see separate grains 100–400 nm in size and small channels between them on the sample surface. No grain damage in the form of cracks or inclusions was observed.

In the image of the mBT surface about 1.5 × 1.5 mm in size (Fig. 1b), it is difficult to distinguish individual particles, which speaks about the absence of a pronounced relief; however, at the stronger magnification (Fig. 1c), grains 30–50 μm in size become visible.

The X-ray diffraction investigations of the nBT and mBT samples were performed at room temperature on a D8-ADVANCE diffractometer (CuK_α radiation, θ–2θ scanning) using a VANTEC linear detector. The 2θ angle scanning step was 0.016° and the exposure was 0.3 s per step. The obtained X-ray diffraction patterns (Fig. 2) were used to refine the structure by the Rietveld method using the TOPAS 4.2 program [20].

All the reflections were reliably identified in the tetragonal lattice (*P*4*mm*) with the parameters similar to those of the $BaTiO_3$ single crystal [21]. This crystal structure was taken as an initial model for the Rietveld refinement. The X-ray diffraction patterns for both samples contained only few low peaks, which can be related to the impurity phases with a mass smaller than 1–2%. The narrow and broad main reflections observed for the micro- and nanoceramics, respectively, are consistent with the expected crystallite size. The estimated average crystallite sizes do have different values (Table 1).

The final refinements of all the parameters appeared stable with the low *R* factor values (Table 1

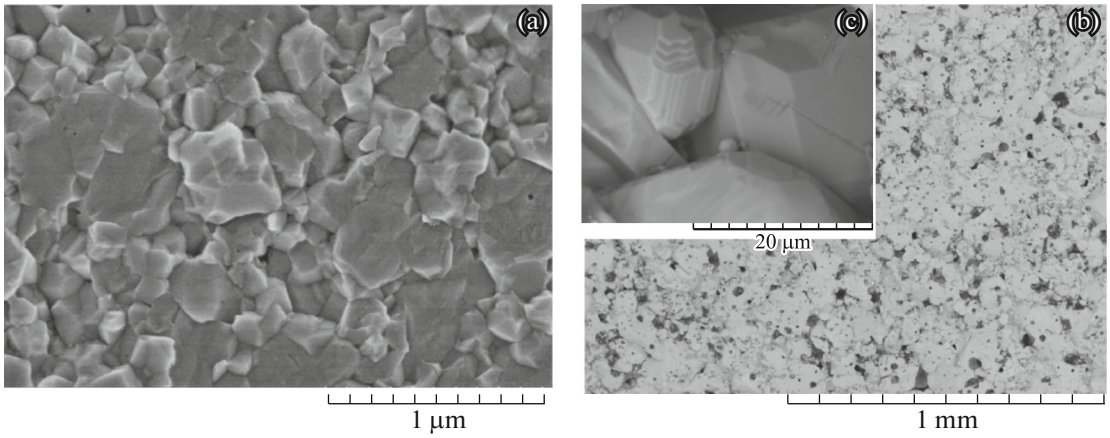

Fig. 1. SEM image of (a) the nBT and (b, c) mBT samples.

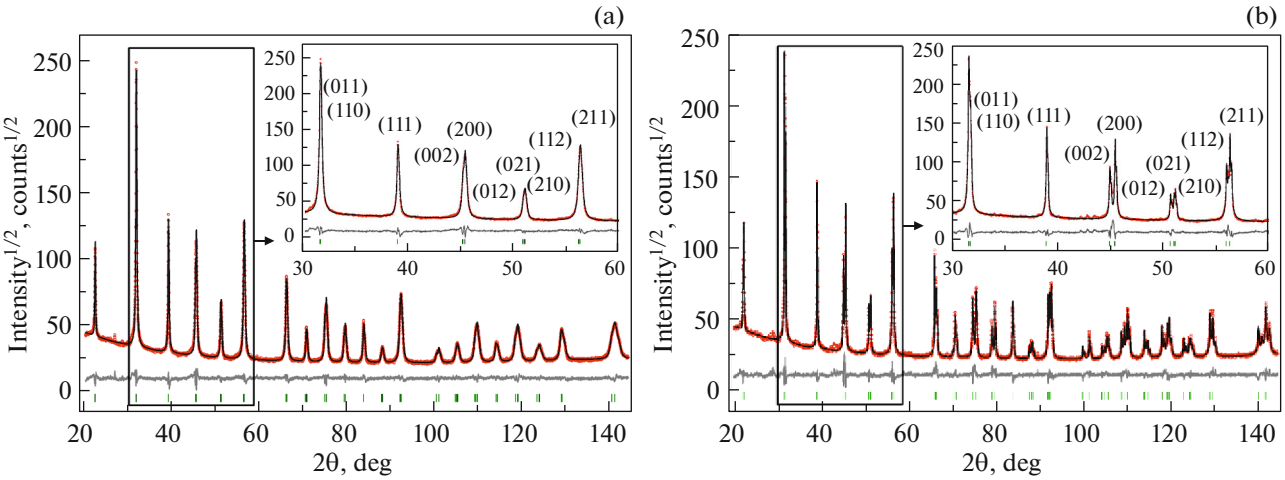

Fig. 2. Difference X-ray diffraction patterns for (a) the nBT and (b) mBT samples.

and Figs. 2a, 2b). It should be noted that the cell parameters of the $BaTiO_3$ micro- and nanoceramic samples are different, which caused an increase in the nBT unit cell volume (Table 1). The analysis of bond lengths showed that the d(Ba–O) distances for both compounds are very similar, in contrast to the d(Ti–O) distances. We may assume that the compositions of the nano- and microcrystalline compounds are different due to the formation of vacancies.

The dielectric properties were measured using an E7-20 device at a frequency of 1 kHz for the nanoceramics and 5 kHz for the microceramics. Gold electrodes were used for nBT and a silver-based conducting paste, for mBT. The measurements were performed in the heating mode at a rate of 0.5–2 K/min in the temperature range of 80–420 K.

The dilatometric investigations were carried out on the ceramic samples with a size of $L \approx 5$ mm using a Netzsch DIL-402C inductive dilatometer in the dry helium gas flow. The sample heating rates in the temperature range of 100–700 K were from 2 to 4 K/min. A fused silica reference was used to calibrate and take into account the expansion of the measuring system. The data obtained in several measurement series were consistent with each other with an error of 2–3%.

The specific heat investigations in the temperature range of 90–430 K were carried out on an automated adiabatic calorimeter described in detail in [22]. The continuous heating rates ranged from 0.01 to 1 K/min and the discrete heating time was from 20 to 40 min. The samples were placed in a cell and fixed with ApiezonN and ApiezonH lubricants, which ensured a reliable thermal contact. To obtain the calorimetric data at high temperatures ($T > 370$ K), the measurements were performed using a Netzsch DSC 204 device.

Table 1. Main results of the processing of X-ray data on nano- and micro-$BaTiO_3$

Compound	nBT	mBT
Sp. gr.	*P4mm*	*P4mm*
a, Å	4.00209 (6)	3.99326 (2)
c, Å	4.01915 (8)	4.03517 (3)
V, Å^3	64.374 (2)	64.3454 (8)
Z	1	1
2θ-interval, deg	20–144	20–144
R_{wp}, %	6.15	8.08
R_p, %	4.73	5.90
R_{exp}, %	2.87	2.98
χ^2	2.15	2.71
R_B, %	1.39	2.93

3. RESULTS AND DISCUSSION

3.1. Permittivity

Figure 3 shows temperature dependences of the permittivity and dissipation factor for the nBT and mBT samples.

In the case of the nanoceramics (Fig. 3a), the permittivity monotonically grows and its peak maximum at a temperature of $T_1 = 399$ K attains giant values (ε = 39600). In the region of three $BaTiO_3$ phase transitions, strongly blurred ε(*T*) anomalies are observed. The dissipation factor in the low-temperature region has a maximum (0.63) at $T = 105$ K, then monotonically decreases to a minimum of ~0.1 in the temperature range of 290–300 K, and starts gradually increasing again to 0.12 at the maximum experimental temperature. It is important that, in the temperature range corresponding to the three phase transitions, there are no features in the dielectric loss plot. This tan(*T*) behavior was observed earlier in the $BaTiO_3$ nanoceramics [23, 24] and corresponds to the temperature activation of the dielectric relaxation. Similar phenomena were found in the well-known CCTO material with a colossal permittivity [25].

The dielectric properties of the microceramics behave completely differently (Fig. 3b). The ε(*T*) dependence contains three anomalies corresponding to the phase transition in $BaTiO_3$. At the temperature $T_1 = 402$ K of the transition between the cubic and tetragonal phases, the maximum permittivity attains ε = 3700. The dielectric loss in the region of the phase transition at $T_2 = 287$ K and $T_1 = 403$ K has the pronounced peculiarities. Near 100 K, similar to the case of nBT, there is a maximum in the tanδ(*T*) dependence. The colossal difference between the ε values and ε(*T*) behaviors for the nano- and microceramics can be caused by the use of different sample fabrication technologies. The SPS process is effective for removal of the resistive component from the grain boundaries, which is usually observed in the conventionally sintered $BaTiO_3$ ceramics, which leads to a significant increase in the permittivity of the SPS nanoceramics [26]. In other words, the high-density (over 98% of the theoretical value) nanoceramics contains a fewer amount of the resistive components as compared with the microceramics and thereby have a lower free charge density at the grain boundaries. In such nanoceramics, a decrease in the grain size does not change the type of carriers, associated mainly with oxygen vacancies, but, during reoxidation, leads to a more significant decrease in the density of such carriers, which affects the transport conductivity mechanism controlled mainly by the grain boundaries [27].

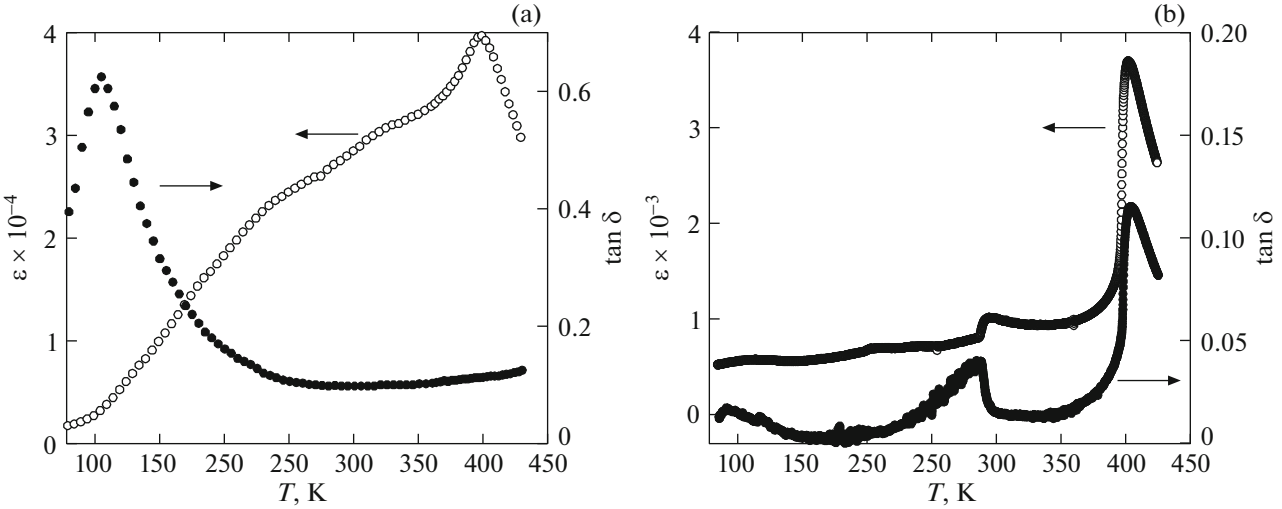

Fig. 3. Temperature dependences of the permittivity and dissipation factor for (a) the $BaTiO_3$ nano- and (b) microceramics.

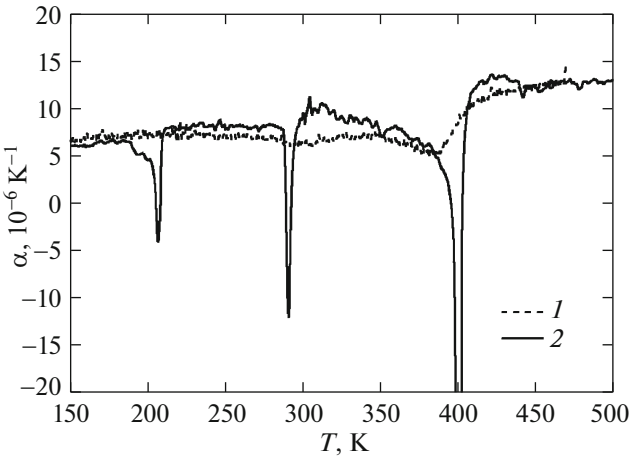

Fig. 4. Temperature dependences of the thermal expansion coefficient for (*1*) the nBT and (*2*) mBT ceramic samples.

3.2. Thermal Expansion

Figure 4 shows the measured data on the thermal expansion of the $BaTiO_3$ micro- and nanoceramic samples. The mBT $\alpha(T)$ anomalies related to the phase transitions $Pm3m-P4mm-C2mm-R3m$ were found at temperatures of $T_1 = 400 \pm 2$ K, $T_2 = 290 \pm 2$ K, and $T_3 = 206 \pm 2$ K and are fairly similar to the temperatures of the transition in the $BaTiO_3$ crystal; the thermal expansion coefficients agree with the data from [28, 29].

It can be seen in Fig. 4 that all the $\alpha(T)$ anomalies in nBT are strongly spread, including especially the anomaly in the region of the low-temperature phase transition $C2mm - R3m$. In addition, a decrease in the particle (grain) size leads to the lowering of the Curie temperature $T_1 = 384 \pm 5$ K for the phase transition $Pm3m-P4mm$. The changes in the temperatures of the phase transitions $P4mm-C2mm$ and $C2mm-R3m$ are not that obvious: $T_2 = 303 \pm 5$ K and $T_3 = 205 \pm 15$ K.

3.3. Specific Heat of the Nano- and Microceramics

Figures 5a and 6a show temperature dependences of the nBT and mBT specific heat in the range of 80–430 K. For nBT, there are several small $C_p(T)$ anomalies with the spread peaks. On the contrary, the mBT data demonstrate three pronounced anomalies. To extract the anomalous specific heat component and calculate the entropy of the phase transitions, we determined the lattice specific heat by approximating the experimental data beyond the region of existence of the anomalies using a combination of the Debye and Einstein functions. The excess specific heats ΔC_p (the difference between the total and lattice specific heats) calculated from these data for nBT and mBT are presented in Figs. 5b and 6b, respectively. The temperature dependences of the anomalous entropy related to the sequential phase transitions were calculated by integrating the function $(\Delta C_p/T)(T)$ (Figs. 5c and 6c).

The comparison of the nBT and mBT data shows that a decrease in the grain size leads to the significant spread of the anomalies related to the phase transitions, narrowing of the temperature region of existence of the tetragonal phase, and a decrease in the phase transition entropy (Table 2). These results are consistent with the data on the size effects in thin films [30]. In study [31], however, the investigations of the specific heat of the nanostructured $BaTiO_3$ ceramics with grain sizes of 50–1200 nm obtained by the force impact combined with shear straining on a Netzsch DSC 204 facility showed a significant (manifold!) increase in the entropy of the phase transformations in the sample consisting of nanoparticles as compared with the sample consisting of microparticles. This entropy (and, consequently, polarization) growth was attributed by the authors to a great number of defects contained in crystallites.

In the repeated measurements, a decrease in the anomalous specific heat (and, consequently, entropy) caused by the temperature annealing of defects was observed. This obvious contradiction of the results forced us to carry out additional investigations on the similar differential scanning calorimeter. Figure 7 presents temperature dependences of the nBT and mBT specific heat.

Table 2 gives the thermodynamic parameters obtained on the adiabatic and differential scanning calorimeters. Generally, the results are in satisfactory

Table 2. Thermodynamic parameters of nBT and mBT obtained on an adiabatic calorimeter and DSC-204

		Cubic ↔ tetragonal		Tetragonal ↔ rhombic		Rhombic ↔ orthorhombic	
		nBT	mBT	nBT	mBT	nBT	mBT
Adiabat	T, K	383 ± 2	396.7 ± 0.5	310 ± 2	286.0 ± 0.5	227 ± 2	201.6 ± 0.1
	ΔS, J/mol K	0.6	1.3	0.25	0.65	0.1	0.23
DSC	T, K	380 ± 5	400.1 ± 0.5	311.0 ± 2	285.6 ± 0.5	222 ± 2	203.3 ± 0.5
	ΔS, J/mol K	–	0.6	–	0.3	1.2 (resulting)	0.2

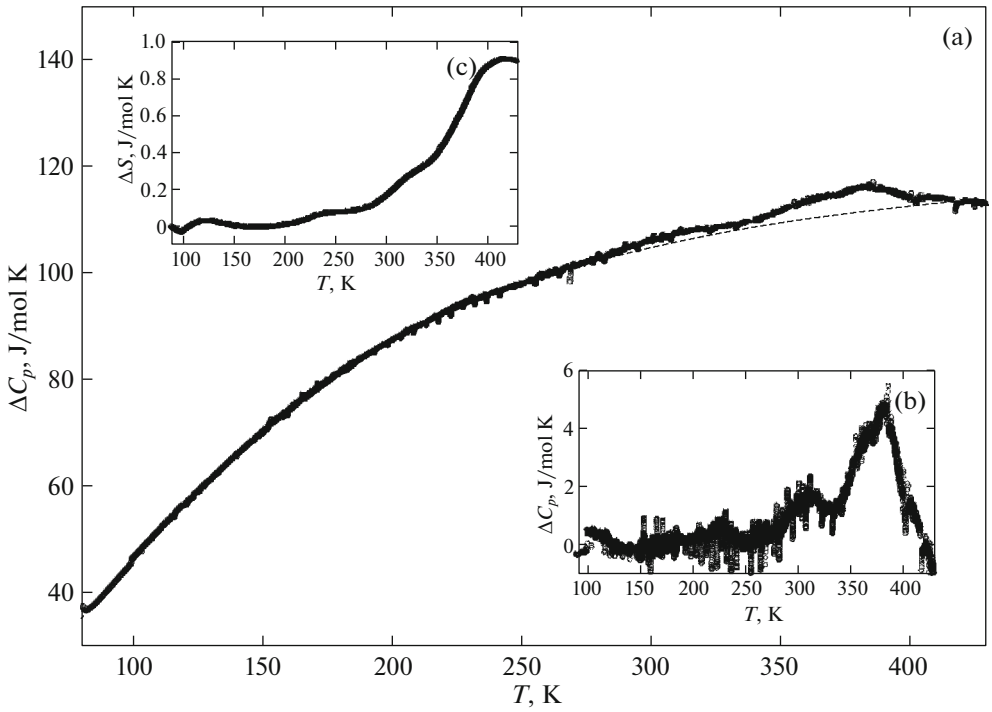

Fig. 5. Temperature dependences of (a) the specific heat, (b) excess specific heat, and (c) entropy for nBT.

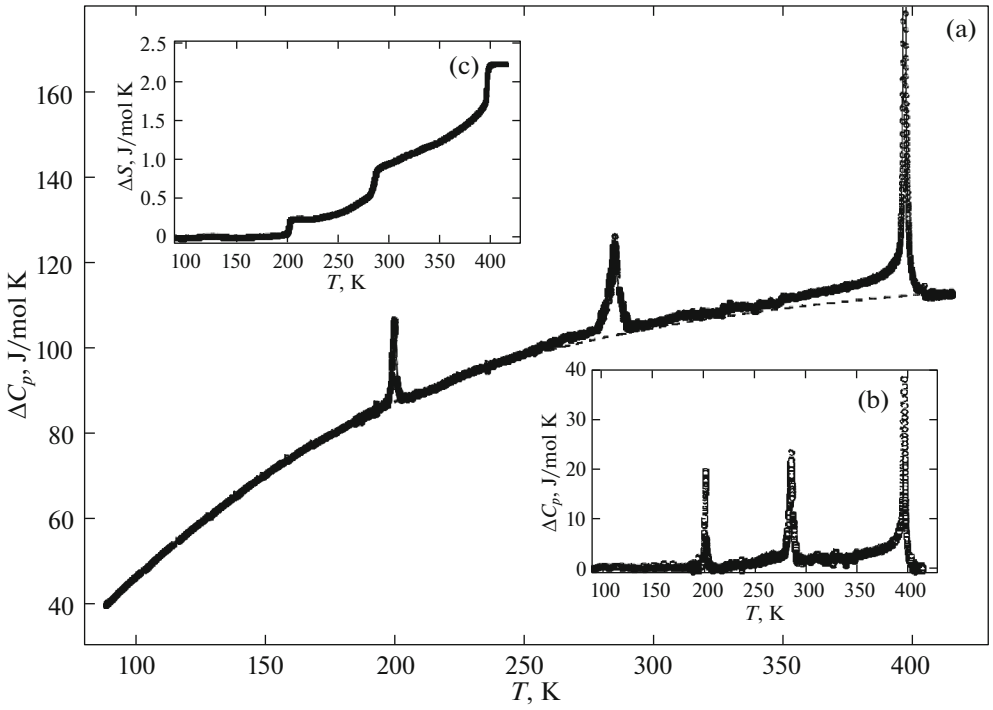

Fig. 6. Temperature dependences of (a) the specific heat, (b) excess specific heat, and (c) entropy for mBT.

agreement. Some differences between the PT temperatures and entropies are caused by the different accuracies and conditions of the measurements on the two facilities.

3.4. Electrocaloric Effect

The size effect was largely manifested in the suppression of the specific heat and thermal expansion

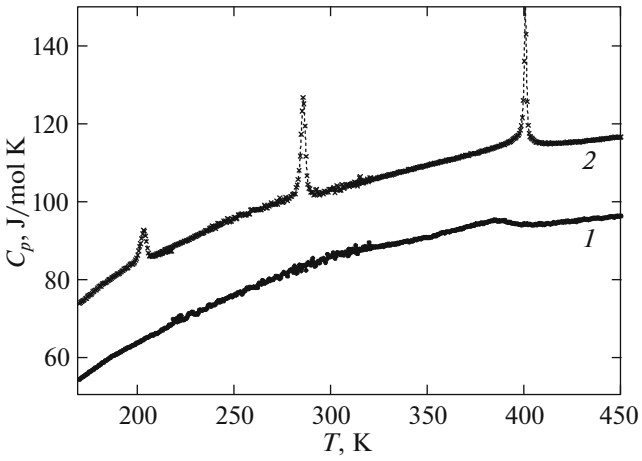

Fig. 7. DSC 204 (Netzsch) temperature dependences of the specific heat for (*1*) the nBT and (*2*) mBT ceramic samples.

anomalies and changes in the temperature and entropy of the phase transitions and permittivity.

The obtained experimental data on the thermal and dielectric properties of the nano- and microceramics are indicative of the pronounced size effect, which manifests itself in a decrease and spread of the phase transition temperature. According to the data from [32, 33], the high permittivity of the nanoceramics as compared with the microceramics should facilitate the implementation of the significant ECE. However, the total excess entropy of the phase transitions in nBT is, first, lower than in mBT, and, second, spread in a wide temperature range, which can lead to a decrease in the ECE value.

The direct measurements of the intense ECE $\Delta T_{AD}(T)$ were performed on an adiabatic calorimeter by the technique used by us earlier in studying the electro- and magnetocaloric effects [22, 34, 35]. The electric field was induced by a stabilized high voltage source. The specific heat of the electrodes and lead wires was lower than 1% of the total specific heat (sample + cell); therefore, the ECE loss on their heating was ignored.

At a certain temperature, the adiabatic calorimeter was tuned so that the sample temperature drift was no worse than $\pm 10^{-3}$ K/min. Such a temperature behavior points out that the conditions established in the cryostat are maximally similar to the adiabatic ones: the system is stabilized in the stable dynamic equilibrium. Then, a voltage pulse with a length of 3–10 min was applied to the sample electrodes, which led to an increase in the sample temperature by means of the ECE. After switching off the field, the sample temperature decreased. The ECE ΔT value was determined as a difference between the temperatures obtained by the linear extrapolation of the $T(t)$ dependences by the instant of switching on/off the field. The error of determination of the ΔT value was no larger than $\pm 2 \times 10^{-4}$ K.

Figure 8 shows time dependences of the temperature for the three series of experiments conducted in the tetragonal phase in the electric field on and off modes.

Near 320 K, the reversibility of the nBT temperature variation is reliably detected (Fig. 8a). However, in the region of 340 K, the sample temperature variation after switching on the field has the higher rate dT/dt than before switching on, but after switching off the field, it returns to the initial rate (Fig. 8b). It can be seen that the sequence of processes $E = 0 \rightarrow E \neq 0 \rightarrow E = 0$ results in the irreversible increase in the sample temperature, which increases with the number of the E on-off cycles. The results of the measurements at two temperatures show that the increase in the rate dT/dt in the applied field is related to the nBT conductivity, which increases with temperature. Thus, at 340 K, we observed the total temperature change caused by the ECE and Joule heat release on the sample resistance.

The temperature splashes during switching on/off the field are related to the peculiarities of temperature control system operation. The values of these effects are smaller than the ECE value, which makes it possi-

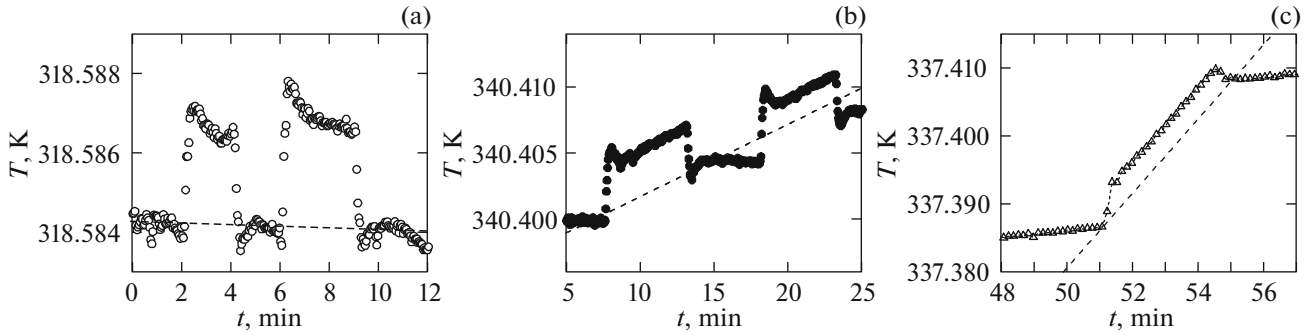

Fig. 8. Temperature behavior variation in an applied electric field as a result of the intensive electrocaloric effect at temperatures of about (a) 320 and (b) 340 K for nBT (2 kV/cm) and (c) 340 K for mBT (2.5 kV/cm).

Table 3. Measured and real electrocaloric effects and spurious heating rate at the instants of switching on the field

Temperature, K		318.584	337.39	340.40	380.1	411.85	419.5
ΔT_{exp}, mK	nBT	2.5	–	3.5	–	16	–
	mBT	–	4.5	–	14	–	10
ΔT_{AD}, mK	nBT	4.2	–	5.9	–	29	–
	mBT	–	15	–	46	–	33
Heating rate, mK/min	nBT	<0.05	–	0.6	–	30	–
	mBT	–	5.0	–	65	–	410

ble to reliably separate them via extrapolating the temperature variations to the E on–off instants.

The additional mBT heating in the applied field due to the Joule heat starts manifesting itself at a lower temperature (Fig. 8c) and, consequently, at a larger distance from the temperature of the phase transition to the cubic phase, as compared with nBT. This makes it even more complicated to distinguish this effect and ECE and reduces the reliability of the results. Table 3 gives the data on the rates of sample heating unrelated to the ECE at several temperatures.

To determine a real value of the intensive ECE ΔT_{AD}, it is necessary to correct the experimentally measured ΔT_{exp} value, since the heat released by means of the ECE is spent to the change not only in the sample temperature, but in the temperature of the entire sample–cell system. The relation between the ΔT_{exp} and ΔT_{AD} values is established by the expression $\Delta T_{AD} = \Delta T_{exp}(1 + C_f/C_{smp})$, where C_{cell} is the cell specific heat determined in a separate experiment and C_{smp} is the specific heat of the sample. The ratios between the ΔT_{AD} and ΔT_{exp} values for nBT and mBT are given in Table 3.

Figure 9 shows temperature dependences of ΔT_{AD} in fields of 2 and 2.5 kV/cm for nBT and mBT, respectively. For both samples, the ECE maxima $\Delta T_{AD}^{max} = 29$ mK at $T^{max} \approx 410$ K (nBT) and $\Delta T_{AD}^{max} = 70$ mK at 380–390 K (mBT) are reliably detected. In nBT, the maximum temperature is significantly higher than the phase transition temperature $T_1 = 383$ K, while in mBT, T^{max} is lower than the corresponding phase transition temperature $T_1 = 396.7$ K. Unfortunately, we could not study the temperature range above 400 K more fully and reliably because of the high conductivity and limited operation temperature ($T < 430$ K) of the adiabatic calorimeter.

3.5. Study of the nBT Conductivity

It is worth noting that the irreversible sample heating by means of the Joule heat was also observed in studying the ECE in single crystals and layered ceramic structures [35, 36]. The relatively high conductivity makes it difficult not only to determine the real value of the effect, but also to use the ferroelectrics as solid-state cooling agents in practice.

Figure 10 shows I–V characteristics for the nanoceramic sample at two temperatures. The obviously nonlinear behavior suggests that the electrical resistance is a function of the applied voltage. This behav-

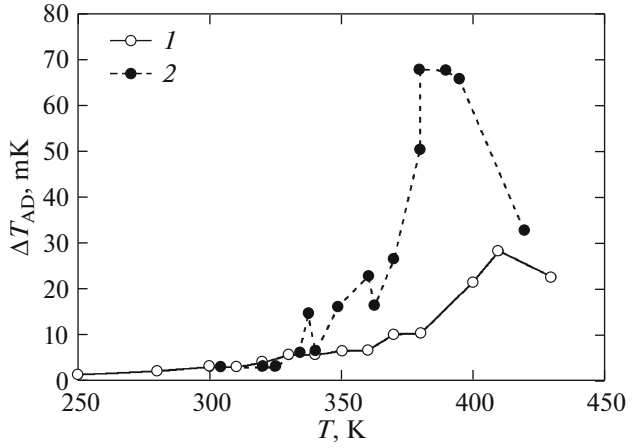

Fig. 9. Temperature dependence of the intensive electrocaloric effect for (*1*) nBT and (*2*) mBT.

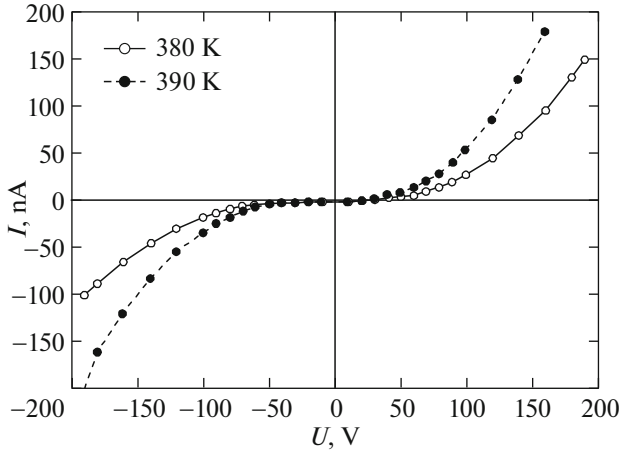

Fig. 10. I–V characteristic for nBT at temperatures of 380 and 390 K.

ior of the electrical resistance originates, as a rule, from the physical processes occurring on the electric contacts with the dielectric and the presence of oxygen vacancies and free charges localized in the intergrain boundaries and in grains as a result of SPS [23, 24, 26]. As was established in [37], the high-density nanoceramics has the *p*-type conductivity in grains and high-resistance intergrain boundaries. Thus, in this material, the effect implemented on the contacts between surfaces is similar to the process occurring on parallel counter-connected *p*–*n* junctions in semiconductors.

4. CONCLUSIONS

Using the adiabatic calorimeter technique, we examined the intensive ECE ΔT_{AD} in the vicinity of phase transitions in the $BaTiO_3$ nano- and microceramics. Some aspects of the influence of methods used for obtaining and thermal processing of the ceramic samples and crystallite size on the thermal, dielectric, and transport properties, as well as on the ECE value and degree of reversibility were studied.

The measurements of the thermal (thermal expansion and specific heat) and dielectric properties of the nano- and microceramics demonstrate a significant spread of the phase transitions in the nanoceramics as compared with the microceramics, which can be related to the smaller grain size in the nanoceramic sample. The total entropy change caused by all the phase transitions in nBT halved as compared with mBT.

The permittivities of the nano- and microceramics are essentially (30 times) different near the high-temperature phase transition. Such a huge difference between $\varepsilon(T)$ is related to the technique used to obtain the ceramics and results from both the oxygen nonstoichiometry of the nanoceramic sample and the presence of free charges at the boundaries of nanograins formed at a fairly low temperature in a rarefied atmosphere during spark plasma sintering.

The results of the direct ECE measurements under adiabatic conditions with and without the electric field at low temperatures and weak electric fields are characterized by the high reproducibility and reversibility of the effect. The experimental conductivity of the nano- and microceramics results in the Joule heat release in the sample and irreversible contribution to the change in its temperature. In our opinion, the presence of the conductivity can be caused by a poor interface between the samples under study and electrodes or oxygen vacancies and free charges localized both in grains and in the grain boundaries. Unfortunately, we failed to implement the ECE in the nanoceramics in strong electric fields because of the high conductivity of the material. The determined nBT and mBT electrocaloric coefficients appeared to be significantly lower than in the single-crystal and polycrystalline $BaTiO_3$ samples [11, 38].

Thus, the results obtained showed that, despite the different methods used to fabricate the $BaTiO_3$ ceramics, their conductivity does not allow one to implement a significant electrocaloric effect in such materials in strong electric fields. However, taking into account that all the data were obtained in weak fields, further investigations of the ceramics with the very low conductivity and high susceptibility to strong electric fields are undoubtedly interesting and promising. The development of new methods for synthesizing such materials will facilitate the creation of caloric elements for cooling systems based on the electrocaloric effect.

REFERENCES

1. Y. Liu, J. F. Scott, and B. Dkhil, Appl, Phys. Rev. **3**, 031102 (2016).
2. Y. Liu, J. F. Scott, and B. Dkhil, Appl. Mater. **4**, 064109 (2016).
3. H. Khassaf, T. Patel, and P. Alpay, J. Appl. Phys. **121**, 144102 (2017).
4. Y. V. Sinyavski, G. E. Lugansky, and N. D. Pashov, Cryogenics **32**, 28 (1992).
5. S. G. Lu, B. Rožič, Q. M. Zhang, Z. Kutnjak, R. Pirc, and M. Lin, Appl. Phys. Lett. **97**, 2291 (2010).
6. X. Hao, Z. Yue, J. Xu, S. An, and C.-W. Nan, J. Appl. Phys. **110**, 064109 (2011).
7. D. Saranaya, A. R. Chaudhuri, J. Parui, and S. B. Krupanidhi, Bull. Mater. Sci. **32**, 259 (2009).
8. A. S. Mischenko, Q. M. Zhang, J. F. Scott, R. W. Whatmore, and N. D. Mathur, Science (Washington, DC, U. S.) **311**, 1270 (2006).
9. S. Kar-Narayan and N. D. Mathur, J. Phys. D **43**, 032002 (2010).
10. N. A. S. Smith, M. K. Rokosz, and T. M. Correia, J. Appl. Phys. **116**, 044511 (2014).
11. X. Moya, E. Stern-Taulats, S. Crossley, D. Gonzolez-Alonso, S. Kar-Narayan, A. Planes, L. Manosa, and N. D. Mathur, Adv. Mater. **25**, 1360 (2013).
12. M. Valant, A.-K. Axelsson, F. Goupil, and N. M. Alford, Mater. Chem. Phys. **136**, 277 (2012).
13. D.-H. Kim, W.-S. Um, and H.-G. Kim, J. Mater. Res. **11**, 2002 (1996).
14. T. Tunkasiri and G. Rujijanagul, J. Mater. Sci. Lett. **15**, 1767 (1996).
15. C. Neusel and G. A. Schneider, J. Mech. Phys. Solids **63**, 201 (2014).
16. Z. Zhao, V. Buscaglia, M. Viviani, M. T. Buscaglia, L. Mitoseriu, A. Testino, M. Nygren, M. Joknsson, and P. Nanni, Phys. Rev. B **70**, 024107 (2004).
17. S. Lin, T. Lu, C. Jin, and X. Wang, Phys. Rev. B **74**, 134115 (2006).
18. B. A. Strukov, S. T. Davitadze, S. N. Kravchun, S. A. Taraskin, M. Golyzman, V. V. Lemanov, and S. G. Shulman, J. Phys.: Condens. Matter **15**, 4331 (2003).
19. Z. Valdez-Nava, S. Guillemet-Fritsch, C. Tenailleau, T. Lebey, B. Durand, and J. Y. Chane-Ching, J. Electroceram. **22**, 238 (2009).

20. *Bruker AXS TOPAS V4: General Profile and Structure Analysis Software for Powder Diffraction Data, User's Manual* (2008).
21. G. H. Kwei, A. C. Lawson, S. J. L. Billinge, and S. W. Cheong, J. Phys. Chem. **97**, 2368 (1993).
22. A. V. Kartashev, I. N. Flerov, N. V. Volkov, and K. A. Sablina, Phys. Solid State **50**, 2115 (2008).
23. C. Voisin, S. Guillemet-Fritsch, P. Dufour, C. Tenailleau, H. Han, and J. C. Nino, Int. J. Appl. Ceram. Technol. **10**, E122 (2013).
24. H. Han, C. Voisin, S. Guillemet-Fritsch, P. Dufour, C. Tenailleau, C. Turner, and J. C. Nino, J. Appl. Phys. **113**, 024102 (2013).
25. M. A. Subramanian, D. Li, N. Duan, B. A. Reisner, and A. W. Sleight, J. Solid State Chem. **151**, 323 (2000).
26. T. Takeuchi, E. B. Etourne, M. Tabuchi, H. Kageyama, Y. Kobayashi, A. Coast, F. Morrison, D. C. Sinclair, and A. R. West, J. Mater. Sci. **34**, 917 (1999).
27. M. Legallais, S. Fourcade, U.-C. Chung, D. Michau, M. Maglione, F. Mauvy, and C. Elissalde, J. Eur. Ceram. Soc. **38**, 543 (2018).
28. Y. He, Thermochim. Acta **419**, 135 (2004).
29. V. Mueller, L. Jager, H. Beige, H.-P. Abicht, and T. Muller, Solid State Commun. **129**, 757 (2004).
30. B. A. Strukov, S. T. Davitadze, V. V. Lemanov, S. G. Shulman, Y. Uesu, and S. Asanuma, Ferroelectrics **347**, 179 (2007).
31. S. Kallaev, Z. Omarov, A. Bakmaev, and K. Abdulvakhidov, Phys. Solid State **55**, 1095 (2013).
32. S. F. Karmanenko, O. V. Pakhomov, A. M. Prudan, A. S. Starkov, and A. Eskov, J. Eur. Ceram. Soc. **27**, 3109 (2007).
33. G. Suchaneck and G. Gerlach, Ferroelectrics **516**, 1 (2017).
34. V. Bondarev, E. Mikhaleva, I. Flerov, and M. Gorev, Phys. Solid State **59**, 1118 (2017).
35. V. Bondarev, I. Flerov, M. Gorev, E. Pogoreltsev, M. Molokeev, E. Mikhaleva, A. Shabanov, and A. Es'kov, Scr. Mater. **146**, 51 (2018).
36. I. Flerov and E. Mikhaleva, Phys. Solid State **50**, 478 (2008).
37. X. Guo, C. Pithan, C. Ohly, C.-L. Jia, J. Dornseiffer, F.-H. Haegel, and R. Waser, Appl. Phys. Lett. **86**, 082110 (2005).
38. A. I. Karchevskii, Sov. Phys. **3**, 2249 (1962).

Translated by E. Bondareva